Unsupervised learning classifies global ocean dynamical regions

Maike Sonnewald*, Carl Wunsch

Massachusetts Institute of Technology, 77 Massachusetts Ave, Cambridge, MA 02139, USA, Harvard University, 26 Oxford Street, Cambridge, MA 02138, USA and The University of Texas at Austin, 201 East 24th Street, Austin, TX 78712,USA

& Patrick Heimbach

The University of Texas at Austin, 201 East 24th Street, Austin, TX 78712,USA and Massachusetts Institute of Technology, 77 Massachusetts Ave, Cambridge, MA 02139, USA

Corresponding author address: Maike Sonnewald, Massachusetts Institute of Technology, 77 Massachusetts Ave, Cambridge, MA 02139, USA.

E-mail: maike_s@mit.edu

ABSTRACT

Global ocean dynamically consistent regions are identified using a barotropic vorticity framework for a twenty-year mean from the Estimating the Circulation and Climate of the Ocean (ECCO) state estimate. Closure of the barotropic vorticity budget provides both classification and dynamical interpretation, highlighting where linear theory is appropriate and where non-linear terms are significant. The unsupervised learning algorithm, K-Means, demonstrates five unambiguous and basin independent global regimes. A "Momentum dominated" area covers $57\pm2\%$ of the ocean area. Surface and bottom stress terms are balanced there by the bottom pressure torque and the non-linear terms. The "Transition zone" covers $18 \pm 0.7\%$, and is found mainly in highly baroclinic subpolar regions. The surface and bottom stress are largely balanced by the Coriolis term and the bottom pressure torque. "Subtropical gyres" cover $11 \pm 0.5\%$, characterized by a "Quasi-Sverdrupian" regime where the Coriolis term is balanced by the wind and bottom stress term. The "Subpolar gyre" region characterised by baroclinic dynamics covers $5.0 \pm 1.9\%$, and is a muted version of the "Transition zone". Similar gyre dynamics are seen in the "Southern Ocean gyre" covering $1.4 \pm 0.7\%$. The shift from the subpolar through the transition zone to the subtropical gyres is a shift from strong interior flow to one dominated by e.g. the western boundary currents. Remaining $6 \pm 0.2\%$ of the area is "Dominantly non-linear", and found in key areas in the Southern Ocean and along western boundaries.

1. Motivation

The global ocean contains diverse dynamic and kinematic regions. This diversity renders difficult forming generalizations and understanding of the global system. A central purpose of this paper is to objectively identify regions of common dynamics as a step towards their understanding. For purposes of exploring appropriate methodologies, the study is restricted to the barotropic vorticity balance of a time-mean global circulation, although it is readily generalized to many other ocean circulation characteristics.

Characterizing the global ocean and reducing the overwhelming dimensionality of observed motions has a long history in oceanography. Using theoretical conjectures, Stommel (1948) and Munk (1950) assumed topography is not important in the subtropics, while topography has been key in understanding Southern Ocean dynamics (Munk and Palmén 1951). From theoretical conjectures and numerical models, it is not obvious what level of complication is merited, or if any useful global description is plausible. General Circulation Models (GCMs) solve the primitive equations in detail, and using the success of simple characterizations of ocean features can be assessed against them. The need for a full GCM approach can be tested regionally, and its success and failure understood in terms of captured key dynamics.

To this end, an "unsupervised learning classification" algorithim is applied here to a depth-integrated, barotropic vorticity (BV) equation. Adequacy of the BV framework is assessed for decadal timescales. The success of work such as Munk (1950) relies on a depth-integrated view, where lateral friction provides closure in what is often referred to as Munk boundary layer structure for Western Boundary Currents (WBC). A quasi-Sverdrupian framework was invoked

by him, where the depth-integrated meridional flow is given by the local wind-stress curl. The potential success of such frameworks suggests predictive skill based purely on the wind field, and that a barotropic, depth-integrated view is appropriate to characterize the subtropical ocean. GCM studies and observational work present a more intricate ocean, where baroclinic structure and non-linearities are key to ocean dynamics. If this complexity is correct for large regions of the ocean, or if they govern key dynamics on relevant timescales, the simplified theoretical view would be inadequate.

The presence of dynamical regimes is suggested by the structures of the wind-stress forcing and the geometry of the ocean basins including the underlying topography. Classifying and identifying regions in the world ocean is done here by using the BV equation and showing that the global budget can be closed. Yeager (2015); Schoonover *et al.* (2016); Le Bras *et al.* (in review) have assessed the dynamics of the BV budget focusing on the North Atlantic. The link to the overturning and gyre circulation, as well as to the importance of mechanisms such as buoyancy forcing were discussed. Here the procedures are global.

Much previous work assessing global ocean dynamics has been constrained to the surface. Xu and Fu (2012) used surface quasigeostrophic theory and sea surface height (SSH) data from altimeters to show differing regimes of geostrophic turbulence. Major current systems have been identified, but with altimeters alone, the application to a comprehensive assessment of global dynamical regimes is limited. Hughes and Williams (2010); Sonnewald *et al.* (2018) use linear statistical models, finding global patterns in SSH. Those global patterns are connected to circulation patterns and planetary waves, and the statistical approach using autoregressive and moving average models was suggestive of global regimes. The present work extends the pattern

determination methodology.

Objective methods to identify patterns in data are common in many fields ranging from pharmaceutical to engineering applications (Kulis and Jordan 2012; Breuhl *et al.* 1999; Hauser and Rybakowski 1997). Applications in the sciences have been investigated both in the prognostic and diagnostic sense (Krasnopolsky *et al.* 2013; Schneider *et al.* 2017).

Objective classification from machine learning has the potential to powerfully simplify the interpretation of ocean dynamics. The objective aspect allows an unbiased assessment of the success of the theoretical framework used, and the dimensionality reduction offered by using a classifier is a potentially very useful approach in physical oceanography. Ardyna *et al.* (2017) applied a similar method to identify regions with distinct biological activity, and Liang *et al.* (in review) used K-Means clustering to identify key regions for data collection to build maps of nitrate in the Southern Ocean. Compared to the more familiar principal component/factor analysis (PCA), the K-Means cluster analysis has an additional "categorical" constraint. PCA and K-Means maximize the same objective function, but are not identical as discussed in the appendix.

2. Methods

a. ECCOv4 State Estimate

The BV equation is used to assess the extent to which we can close this budget in the version 4 Estimating the Circulation and Climate of the Ocean (ECCOv4) release 2 estimate described by Wunsch and Heimbach (2013); Forget *et al.* (2015) and others (see also ECCO Consortium

(2017a,b)). The state estimate is global 1° with tropical and high latitude mesh refinement. A least-squares with Lagrange multipliers approach is used to obtain the state estimate. The result is a *free-running* version of the MIT General Circulation Model (MITgcm, Adcroft *et al.* (2004))—with adjusted input variables—solving the primitive equations. In contrast to most "reanalysis" products, the ECCO oceanic state satisfies basic conservation laws for enthalpy, salt, volume, and momentum remaining largely within error estimates of a diverse set of global data (Wunsch and Heimbach 2007, 2013; Stammer *et al.* 2016). Regions without data are filled in a dynamically consistent way using the dynamics, avoiding the use of untested statistical hypotheses e.g., Reynolds *et al.* (2013).

b. Barotropic Vorticity

To classify the ocean's dynamical regions the BV equation is used, one based on the solutions to the primitive equations from the ECCOv4 state estimate. Illustrating the simplification, the familiar momentum equations of an ocean on a thin shell on a rotating sphere are:

$$\partial_t \mathbf{u} + f\mathbf{k}\times\mathbf{u} = -\frac{1}{\rho_0}\nabla p + \frac{1}{\rho_0}\partial_z \tau + \mathbf{a} + \mathbf{b}, \partial_z p = -g\rho, \nabla\cdot\mathbf{v} = 0. \tag{1}$$

The pressure, acceleration due to gravity, density and vertical shear stress are denoted p, g, ρ and τ respectively, with ρ_0 the reference density; the three dimensional velocity field $\mathbf{v}$ = (u, v, w) = ($\mathbf{u}$, w); the unit vector is denoted $\mathbf{k}$; planetary vorticity as a function of latitude ϕ in $f\mathbf{k} = (0,0,2\Omega sin\phi)$; the viscous forcing by vertical shear is denoted $\partial_z\tau$; the non-linear terms are $\mathbf{a}$ and the horizontal viscous forcing $\mathbf{b}$ includes subgridscale parameterizations. Assuming a steady state, the vertical integral from the surface $z = \eta(x,y,t)$ to the water depth below the surface $z = H(x,y)$ gives

$$\beta V = \frac{1}{\rho_0}\nabla p_b \times \nabla H + \frac{1}{\rho_0}\nabla \times \tau + \nabla \times \mathbf{A} + \nabla \times \mathbf{B}, \tag{2}$$

where $\nabla \cdot \mathbf{U} = 0, \mathbf{U} \cdot \nabla f = \beta V$, the bottom pressure is denoted p_b, $\mathbf{A} = \int_H^\eta \mathbf{a} \mathrm{d}z$ and $\mathbf{B} = \int_H^\eta \mathbf{b} \mathrm{d}z$. The LHS of equation (2) is the planetary vorticity advective term, while the RHS of equation (2) is the bottom pressure torque (BPT), the wind and bottom stress curl, the non-linear torque and the viscous torque, respectively. The non-linear torque is composed of three terms:

$$\nabla \times \mathbf{A} = \nabla \times \left[\int_{-H}^{0} \nabla \cdot (\mathbf{uu}) \mathrm{d}z \right] + [w\boldsymbol{\zeta}]_{z=H}^{z=0} + [\nabla w \times \mathbf{u}]_{z=H}^{z=0}. \tag{3}$$

The RHS on equation (3) represents the curl of the vertically integrated momentum flux divergence, the non-linear contribution to vortex tube stretching and the conversion of vertical shear to barotropic vorticity. Horizontal viscous forcing includes that induced by subgridscale parameterizations. Twenty-year averaged fields of the BV equation are used after a Laplacian smoother is applied.

c. Unsupervised learning: K-Means clustering

Assessing the presence of dominant global patterns of dominant terms in the BV equation, K-Means clustering is used. In that approach, no groups are prescribed and the data are not constrained, something that otherwise is a first step in oceanographic analysis. K-Means clustering originates in signal processing, and is used to determine if discernible patterns exist in the variations of the data. Patterns of variability constitute areas in a function space, given by the terms of the BV equation, that are more densely populated than others. If groups of dominant terms are present that differ significantly, they are robustly identified and are called "clusters". The spatially varying terms in the BV equation were scaled to have zero mean and unit variance globally. The

algorithm involves an interative minimization of the sum of squares of the Euclidian distance given by the partitioning of the hyperspace:

$$J = \Sigma_{j=1}^{\mathrm{K}} \Sigma_{i=1}^{n} ||x_i^j - c_j||^2 \tag{4}$$

where the number of K (c_j) is a parameter fixed a priori, randomly scattered among the n data points (x). The distance between a data point x_i^j and c_j is given by $||x_i^j - c_j||^2$. Initially, each data point is associated with the closest K cluster. The position of c_j is recalculated, and the association reassessed. This procedure is iteratively repeated. The problem is computationally NP-hard, and sensitive to the initialization and choice of K. As detailed in the Appendix, the appropriate value of K is determined as K>35 using the Akaike and Bayesian Information Criteria (AIC and BIC). The AIC and BIC indicate robust regimes as they both have asymptote, suggesting no information is gained increasing K. A fixed K=50 is used for the remaining analysis. The physical meaning of the K parameter is associated to the variance structure of the data. The algorithm partitions the parameter subspace using linear hyperplanes. The linearity constraint means that higher numbers of K can both assist in partitioning the subspace more appropriately, and also isolate noise. The appendix demonstrates the small sensitivity to the initial random seed of the algorithm, as well as the impact of varying K.

3. Results

Figure 1 illustrates the closure in ECCOv4 for the 20-year average of the BV terms in equation (2). Individual terms are of order $\pm 10^{-9} ms^{-1}$ and the residuals have magnitudes $<<$ 1% for 36% of the ocean—-a very small value (Figure 1), less than $\pm 10^{-12} ms^{-1}$. These small residuals permit going forward with confidence. Some numerical issues do exist on the shelf and in shallow water

generally, but these only amount to 2.9% of the area of the global ocean and will be ignored.

Figure 1b illustrates where the Coriolis term is important in ECCOv4 for the 20-year average from equation (2). This term is balanced by the wind and bottom stress BV terms shown in Figure 1d (the bottom stress term is small) and BPT shown in Figure 1c. The remainder is largely found in the non-linear BV contributions seen in Figure 1e, with the lateral viscous dissipation largely being an order of magnitude smaller, apart from in localized regions in the Southern Ocean.

The wind and bottom stress BV term in Figure 1d are largely zonally symmetric in the 20-year average, with large patterns of negative BV to the south in the Southern Ocean, large gyre patterns visible in the Pacific and Atlantic basins. The BPT term in Figure 1c is associated with interactions with steep bathymetry. For example, in the Southern Ocean a large positive patch leads towards the Antarctic-Pacific ridge, and with a negative patch beyond. This structure is consistent with vortex stretching as the ridge is crossed, and a similar feature is associated with the Mid-Atlantic Ridge in the Atlantic sector of the Southern Ocean. Along Western Boundaries, BPT is positive to the west and negative just adjacent to the east, consistent with studies such as Myers *et al.* (1996). The BV of the non-linear terms is similarly concentrated along the western edge of basins where WBCs are found, but it is less spatially coherent than the BPT term. The Southern Ocean stands out as a region of high activity, particularity in the Atlantic sector. Lateral viscous dissipation in the BV equation is comparatively small, but also concentrated in the Southern Ocean.

Figure 2 illustrates the spatial extent of the dynamical regimes picked out by the K-Means algorithm. The numbering on the colorbar is arbitrary, and the structure is mainly found in five geographically coherent patches named in Table 1. We use these names in the remaining

description. A zonal pattern suggests the wind-stress contribution to the BV is key, but much zonal spatial structure appears in the Southern Ocean and along the western boundaries. Figures 3 and 4 isolate the geographical area and the associated area-averaged magnitudes of the terms in the BV equation, ordered in decreasing percentage coverage of the global ocean. The bar charts represent the area-averaged balance of the terms in the BV equation from the spatial areas determined as distinct by the clustering. Table 1 summarizes the results, listing the corresponding figure and dominant terms in the BV equation found in clusters.

Figure 3a illustrates the region dominated by a balance of the surface and bottom stress terms covering 56% of the global ocean (Cluster 1). This balance suggests a barotropic regime dominated by an apparent "Depth coherent" structure from surface to bottom, and it is found in zonal streaks in the tropics, and a thin ribbon in the Southern Ocean notably in the Pacific sector. In the Northern Hemisphere, Cluster 1 areas surround the subtropical and subpolar gyres. Large areas of the Arctic Seas are also in this Cluster. Figure 3b demonstrates the balance of terms that made the K-Means algorithm pick out the various regions. Wind and bottom stress terms are the major source of negative barotropic vorticity, while the BPT adds positive vorticity. Non-linear terms add negative vorticity.

Figure 3c illustrates the spatial region covering the next largest dynamical region covering 18% of the ocean area (Cluster 2: "Transition zone"). In the Northern Hemisphere, this cluster covers the southern region of the subpolar gyres. A zonal streak crosses the equator in both the Atlantic and Pacific, but is absent in the Indian Ocean. The Southern Hemisphere has large Cluster 2 expanses in both the Pacific and Atlantic, but again not in the Indian Ocean. The bar chart in Figure 3d highlights, as expected, the wind as the major source of barotropic vorticity, with sinks

in the Coriolis term and BPT. A small sink appears in the non-linear terms.

Figure 3e illustrates the 11% of the ocean area selected by the next Cluster (3: "Subtropical gyre"). The subtropical gyres in the Northern Hemisphere Atlantic and Pacific stand out, together with thin streaks on the Equator. Isolated streaks are seen in the Southern Ocean, and in a large area of the Southern Hemisphere tropical Indian Ocean. Figure 3f shows a dominant balance between the input of barotropic vorticity from the Coriolis term and sinks in the wind and bottom stress. This balance corresponds to a quasi-Sverdrupian regime in the depth integrated ocean.

Figure 4a shows the area covered by Cluster 4 covering 7% of the ocean ("Subpolar gyre"). This Cluster is largely a complimentary poleward extension to the cluster covering 18% of the ocean seen in Figure 3c. In the Northern Hemisphere, the Cluster largely represents the northern edge of the subpolar gyre. In the Southern Hemisphere, it is found on the eastern edge of the Pacific and Atlantic basins, just to the south, and flaring out westwards of the continental barrier. In the Indian Ocean, this barrier can be seen to be New Zealand or Australia, and the area of this dynamical regime fills the subtropical Indian Ocean down to the border with the Southern Ocean, where this regime is absent. Figure 4b illustrates that it is an amplified version of the dominant terms seen in figure 3d, being an order of magnitude larger, but still having the wind as the major source of barotropic vorticity with sinks in the Coriolis term and BPT. A small source exists in the non-linear terms.

The Southern Ocean is better represented in the area covering 2% of the global world ocean seen in Figure 4c (Cluster 5: "Southern Ocean gyre"), as seen mainly in a series of streaks in the Southern Ocean, near 60°S where there is no continental block. Isolated areas are also seen in the

Northern Hemisphere. Figure 4d illustrates that this region, Cluster 5 is approximately an inverse of the barcharts for the area representing the Northern extension of the subtropical gyres covering 7% of the world ocean. The wind is the major sink of barotropic vorticity, with sources in the Coriolis term and BPT. Again, non-linear terms are a small sink.

Figure 4e is a summary of the area of the remaining terms that account for 6.3% of the world ocean ("Dominantly non-linear"). Areas of rough bathymetry stand out, such as the Pacific-Antarctic Ridge and the Drake Passage area. Figure 4f illustrates that the non-linear contribution to the barotropic vorticity dominates, together with the Coriolis term. The different constituents are quite varied, but strong contributions from the non-linear terms are consistently present. Such regions will be discussed in a subsequent paper.

4. Discussion and Conclusions

The barotropic vorticity (BV) equation in a 20-year average state estimate is analyzed for the world ocean. Figure 1 shows that the global ocean has large regions of coherent dynamical term balances as displayed in Figure 5. Those balances are nuanced among the wind-stress, Coriolis and bottom pressure torque (BPT) terms. Areas where the non-linear terms are small suggest that the linearized BV is a good approximation. Areas where the non-linear terms are important are found in western boundary regions, as well as the Southern Ocean where the Antarctic Circumpolar Current interacts with bathymetric obstacles. The momentum dominated area implies a coherent vertical structure. The subtropical gyre is unique in lacking significant contributions by BPT. The transition zone has a stronger momentum driven portion of the BPT, and topographic interactions begin to become important. The subpolar gyre has a stronger

baroclinic component to the BPT and feels topography. The Southern Ocean gyre is like the subpolar one, but with contributions of opposite sign. The remaining ocean has important by non-linear contributions, and the linearized barotropic interpretation is not appropriate.

Consistent with the Yeager (2015) analysis in the North Atlantic Ocean, there is a region with a shift from strong interior flow (baroclinic meridional, North Atlantic Current, NAC, and North Atlantic Deep Water, NADW, flow over the Mid Atlantic Ridge) to a more barotropic flow (deep western boundary current, DWBC). The geographical extent and transition between the 18% (Transition zone) and 11% (subtropical) areas make sense as they are mirror images of each other, but with the difference in wind sign and BPT interactions. The 5% (Subpolar gyre) region complements the subtropical region, being an intensified extension having small contributions of non-linear terms. In the global picture, strong interior flow is present in vast expanses of the Southern Hemisphere, as well as in the North Pacific. The quasi-Sverdrupian regime in the Northern Hemisphere subtropics is virtually absent in the South Pacific, consistent with the absence of a strong barotropic flow structure.

The relative sizes of the Clusters need not imply their relative importance in the global circulation. Areas collected here as"Dominantly non-linear" have a small spatial extent, but are found in regions that are known to be important for ocean dynamics. The Drake Passage region as well as the Antarctic-Pacific Ridge are areas where the circulation interacts with topography, and these regions are places where non-linear effects are large. Similarly in the Northern Hemisphere, areas in the Labrador sea and shelf stand out as non-linear.

The sign and spatial distribution of the wind-stress term suggests the importance of Ekman pumping(negative)/suction(positive). The equatorial and Southern Ocean regions show Ekman pumping, while the subpolar gyre areas have Ekman suction where mode waters are created. The BPT term mirrors the wind-stress term, suggesting it acts as either a source or a sink in opposite complement to the wind-stress. A full description of the dynamics is outside the scope of the current study.

K-Means clustering is not the only method for determining regions of dynamical commonality; generalised gaussian mixture models are another possibility. Also, other covariance shapes can be explored, with some initial results in figure 8. Results are little changed, but they may be an important element in moving to higher resolution estimates.

Summary

The barotropic vorticity equation closes very accurately in the 20-year time-average ECCOv4 state estimate. Balances observed involve the three dominant terms of the wind, Coriolis and bottom pressure torque terms, with significant covariance and input from the non-linear terms in some regions. Clusters of similar dynamics were identified using the K-Means clustering method. Five regions cover 93% of the world ocean: depth coherent (57%), transition zone (18%), subtropical gyre (11%), subpolar gyre (5%) and the Southern Ocean gyre (1.4%). The residual area is dominated by the non-linear terms and will be the subject of a future study.

5. Acknowledgments

This work was funded by the US National Aeronautics and Space Administration Sea Level Change Team (contract NNX14AJ51G) and through the ECCO Consortium funding via the Jet Propulsion Laboratory. MS acknowledges the advice and support of Anne Reinarz, Edward Doddridge, Roosa Tikkanen and Katherine Rosenfeld.

K-Means and influence of Information Criteria

The K-Means algorithm is related to methods such as PCA, more traditionally applied to oceanography. Where PCA attempts to represent all data vectors using a low order combination of eigenvectors, minimizing the mean squared reconstruction error, the K-Means algorithm represents the datavectors via a small number of clusters. This is also done to minimize the mean squared reconstruction error. In this manner, the K-Means algorithm can be interpreted as a very sparse PCA.

The K-Means algorithm is initiated by scattering K first-guesses of where the parameters/clusters could be. This initial guess introduces a stochastic element. The success of the algorithm is sensitive to K, as this determines how the hyperspace given by the dimensions is partitioned. As with regression analysis, adding parameters can increase the accuracy, but overfitting should be avoided. To determine the appropriate value of K, the Akaike and Bayesian Information Criteria (AIC and BIC) are used, minimizing the expectation of the prediction error:

$$\mathrm{AIC} = 2K - 2\ln(\mathscr{L}),$$

$$\mathrm{BIC} = Kln(n) - 2ln(\mathscr{L}),$$

where n is the number of datapoints and $\mathscr{L}$ is the likelihood:

$$\mathscr{L} = \Pi_{i=1}^{N} \frac{1}{\sqrt{2\pi\sigma^2}} \exp\left(-\Sigma_{i=1}^{N} \frac{(\zeta_i - \hat{\zeta}_i)^2}{2\sigma^2} \right).$$

ζ_i is the observed, and $\hat{\zeta}_i$ is the prediction, so $(\zeta_i - \hat{\zeta}_i)^2$ are the prediction residuals. In the estimate, the AIC value is minimized, which determines the smallest appropriate order to represent the time-series. As discussed by Priestley (1981) and Yang (2005), the AIC can overestimate the order. Figure 6 demonstrates that both the AIC and BIC stabilise at $> 35K$, and the asymptotic nature of the regime.

Robustness of the regions in terms of the stochastic initialisation is highlighted in Figure 7, where the K-Means clustering was run 100 times. The mean and 2σ are used in Table 1. The regimes identified are robust, with the extent of the subpolar gyre being the main area where the algorithm shows appreciable variance.

To elucidate the impact of assumptions the algorithm makes for the classification, a more generalised form of clustering is also tested: Gaussian Mixture Models. For context, K-Means clustering is the limit where all covariances are diagonal, small and equal. Gaussian Mixture Models are used to assess the impact of assumptions relating to the covariance structure; spherical, diagonal, tied or full covariance are assessed as seen in Figure 8. Using the BIC to assess the impact, this is found to likely to much change present results, but it could be important at higher resolution high resolution, as the K-Means clustering problem is NP-hard.

References

Adcroft, A., Hill, C., Campin, J. M., Marshall, J., & Heimbach, P. (2004). Overview of the formulation and numerics of the MIT GCM (pp. 139-150). Presented at the ECMWF Conference Proceedings, Shinfield Park, Reading, UK.

Akaike, H. (1973), "Information theory and an extension of the maximum likelihood principle", in Petrov, B.N. ; Cski, F., 2nd International Symposium on Information Theory, Tsahkadsor, Armenia, USSR, September 2-8, 1971, Budapest: Akadmiai Kiad, p. 267-281.

Ardyna, M., H. Claustre, J. Sallee, F. DOvidio, B. Gentili, G. van Dijken, F. DOrtenzio, and K. R. Arrigo, 2017: Delineating environmental control of phytoplankton biomass and phenology in the southern ocean. Geophys. Res. Lett., 44, 50165024, doi:10.1002/2016GL072428.

Breuhl S, et al. (1999). Use of clusters analysis to validate IHS diagnostic criteria for migraine and tension-type headache. Headache; 39(3):181-9. A study of validating diagnostic criteria using k-means on symptom patterns.

Church, J.A., et al., 2013: Sea Level Change. In: Climate Change 2013: The Physical Science Basis. Contribution of Working Group I to the Fifth Assessment Report of the Intergovernmental Panel on Climate Change [Stocker, T.F., D. Qin, G.-K. Plattner, M. Tignor, S.K. Allen, J. Boschung, A. Nauels, Y. Xia, V. Bex and P.M. Midgley (eds.)], Chapter 13, pp. 1137-1216, Cambridge University Press.

ECCO Consortium, 2017a, A Twenty-Year Dynamical Oceanic Climatology: 1994-2013. Part 1: Active Scalar Fields: Temperature, Salinity, Dynamic Topography, Mixed-Layer Depth, Bottom Pressure.

ECCO Consortium, 2017b, A Twenty-Year Dynamical Oceanic Climatology: 1994-2013. Part 2: Velocities, Property Transports, Meteorological Variables, Mixing Coefficients.

Forget, G., J.-M. Campin, P. Heimbach, C. N. Hill, R. M Ponte, and C. Wunsch, ECCO version 4: an integrated framework for non-linear inverse modeling and global ocean state estimation, Geo. Sci. Model Dev., 8, 2015

Hauser J and Rybakowski J (1997). Three clusters of male alcoholics. Drug Alcohol Depend; 48(3):243-50. An example of clustering behavior types in addiction research.

Hirschi, J. J.-M., Blaker, A. T., Sinha, B., Coward, A., de Cuevas, B., Alderson, S., and Madec, G.: Chaotic variability of the meridional overturning circulation on subannual to interannual timescales, Ocean Sci., 9, 805-823, doi:10.5194/os-9-805-2013, 2013.

Chris W. Hughes, Simon D. P. Williams, The color of sea level: Importance of spatial variations in spectral shape for assessing the significance of trends, Journal of Geophysical Research, 2010, 115, C10

Vladimir M. Krasnopolsky, Michael S. Fox-Rabinovitz, and Alexei A. Belochitski, "Using Ensemble of Neural Networks to Learn Stochastic Convection Parameterizations for Climate and Numerical Weather Prediction Models from Data Simulated by a Cloud Resolving Model," Advances in Artificial Neural Systems, vol. 2013, Article ID 485913, 13 pages, 2013. doi:10.11552013485913

Kulis, B., Jordan, M. I.Revisiting k-means: new algorithms via Bayesian nonparametrics, Proceedings of the 29th International Conference on Machine Learning (ICML '12)July 2012 Edinburgh, UK5135202-s2.0-84867132578

Le Bras, I., Toole, J.M., Sonnewald, M.: A bulk Potential Vorticity budget for the western North Atlantic based on observations. In review.

Liang, Y.-C. *et al.*, in review.

J. B. MacQueen (1967): "Some Methods for classification and Analysis of Multivariate Observations, Proceedings of 5-th Berkeley Symposium on Mathematical Statistics and Probability", Berkeley, University of California Press, 1:281-297.

Munk, W., 1950: On the wind-driven ocean circulation. J. Meteor., 7, 7993, doi:10.1175/1520-0469(1950)007¡0080:OTWDOC¿2.0.CO;2.

Munk, W.H., and Palmén, E,: Note on the dynamics of the Antarctic Circumpolar Current, Tellus, 3, 53-55, 1940.

Myers, Paul G., Augustus F. Fanning, Andrew J. Weaver, 1996: JEBAR, Bottom Pressure Torque, and Gulf Stream Separation. J. Phys. Oceanogr., 26, 671683. doi: http://dx.doi.org/10.1175/1520-0485(1996)026<0671:JBPTAG>2.0.CO;2

Priestley, M. B. (1981) Spectral Analysis and Time Series, London: Academic Press.

Reynolds, R.W., D.B. Chelton, J. Roberts-Jones, M.J. Martin, D. Menemenlis, and C.J. Merchant, 2013: Objective Determination of Feature Resolution in Two Sea Surface Temperature Analyses. J. Climate, 26, 2514-2533, https://doi.org/10.1175/JCLI-D-12-00787.1

Schoonover, J., Dewar, W., Wienders, N., Gula, J., McWilliams, J.C., Molemaker, M.J., Bates, S.C., Danabasoglu, G. and Yeager, S.: North Atlantic Barotropic Vorticity Balances in Numerical Models, Journal of Physical Oceanography 2016 46:1, 289-303

Lan, S., Schneider, T., Stuart1and, A., and Teixeira, J. (2017). Earth System Modeling 2.0: A Blueprint for Models That Learn From Observations and Targeted High-Resolution Simulations.

Sonnewald, M., C. Wunsch, and P. Heimbach, 2018: Linear Predictability: A Sea Surface Height Case Study. J. Climate, 31, 25992611, https://doi.org/10.1175/JCLI-D-17-0142.1

Stainforth, D., Aina, T., Christensen, C., Collins, M., Faull, N., Frame, D., Kettleborough, J., Knight, S., Martin, A., Murphy, J., Piani, C., Sexton, D., Smith, L., Spicer, R., Thorpe, A. and Allen, M.: 2005, Uncertainty in predictions of the climate response to rising levels of greenhouse gases, Nature 433(7024), 403-406. url:http://oro.open.ac.uk/5025/

D. Stammer, M. Balmaseda, P. Heimbach, A.Koehl, and A. Weaver, 2016: Ocean Data Assimilation in Support of Climate Applications: Status and Perspectives. Ann. Rev. Mar. Sci., 8, 491-518.

Stommel, H. (1948), The westward intensification of wind-driven ocean currents, Eos Trans. AGU, 29(2), 202206, doi:10.1029/TR029i002p00202.

Yang, Y. (2005), "Can the strengths of AIC and BIC be shared?", Biometrika, 92: 937-950, doi:10.1093/biomet/92.4.937.

Yeager, S.: Topographic coupling of the Atlantic overturning and gyre circulations, J. Phys. Oceanogr., 45, 1258-1284. doi: http://dx.doi.org/10.1175/JPO-D-14-0100.1, 2015.

Wunsch, C., and P. Heimbach, 2007: Practical global oceanic state estimation. Physica D, 230, 197-208.

Wunsch, C. and P. Heimbach, 2013, Dynamically and kinematically consistent global ocean circulation and ice state estimates. In Ocean Circulation and Climate 2nd Edition, Siedler et al., Eds.

Wunsch, C. The interpretation of short climate records, with comments on the North Atlantic and Southern Oscillations. Bull. Am. Met. Soc. 80, 245-255 (1999).

Wunsch, C. (2013), Covariances and linear predictability of the Atlantic Ocean, Deep Sea Res., Part II, 85, 228-243.

Wunsch, C. (2015), Modern Observational Physical Oceanography: Understanding the Global Ocean. Princeton University Press.

Xu, Y. and L. Fu, 2012: The Effects of Altimeter Instrument Noise on the Estimation of the Wavenumber Spectrum of Sea Surface Height. J. Phys. Oceanogr., 42, 22292233, https://doi.org/10.1175/JPO-D-12-0106.1

LIST OF TABLES

Cluster	Area	Leading terms
1	57±1.8%, Depth coherent (Fig. 3a)	$\nabla \times \tau_{sb} + \nabla \times \mathbf{A} \approx \nabla p_b \times \nabla H$ (Fig. 3b)
2	18±0.7%, Transition zone (Fig. 3c)	$\nabla \times \tau_{sb} \approx \nabla p_b \times \nabla H + \nabla \cdot (f\mathbf{U})$ (Fig. 3d)
3	11±0.5%, Subtropical gyre (Fig. 3e)	$\nabla \times \tau_{sb} \approx \nabla \cdot (f\mathbf{U})$ (Fig. 3f)
4	5.0±1.9%, Subpolar gyre (Fig. 4a)	$\nabla \times \tau_{sb} \approx \nabla \cdot (f\mathbf{U}) + \nabla p_b \times \nabla H$ (Fig. 4b)
5	1.4±0.7%, Southern Ocean gyre (Fig. 4c)	$\nabla \times \tau_{sb} \approx \nabla \cdot (f\mathbf{U}) + \nabla p_b \times \nabla H$ (Fig. 4d)
6-50	5.7 ± 0.2%, Dominantly non-linear (Fig. 4e)	$\nabla \cdot (f\mathbf{U}) \approx \nabla \times \mathbf{A} + \nabla \times \tau_{sb}$ (Fig. 4f)

TABLE 1: Percentage of area covered by the area specific balance of the BV equation (2) and the corresponding map figure. Leading order terms are sorted by magnitude, colors indicating if barotropic vorticity is added (red) or removed (blue) by the leading order term, the corresponding bar chart figure shows the full breakdown. The quoted percentage coverage and StD is the mean of 100 runs of the algorithm.

LIST OF FIGURES

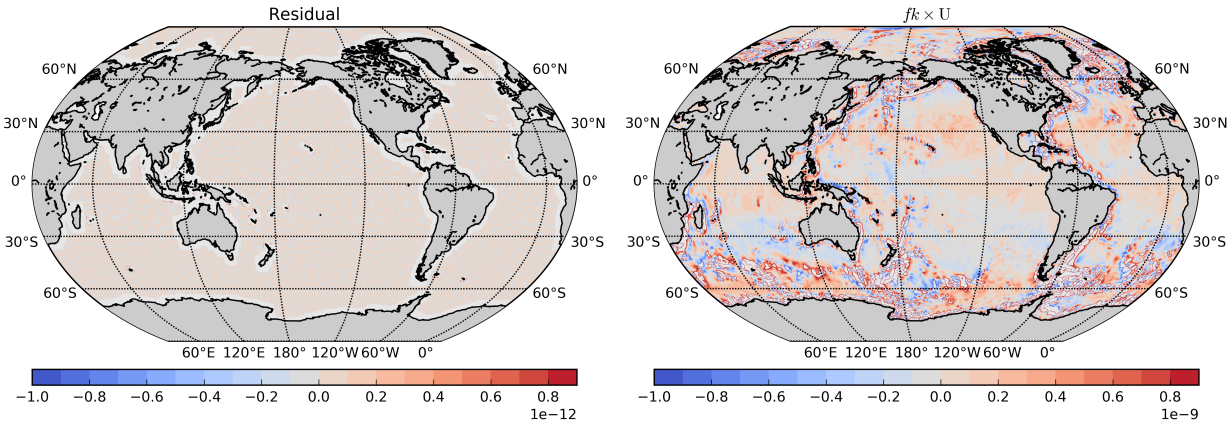

(a) Residual

(b) $\nabla \cdot (f\mathbf{U})$

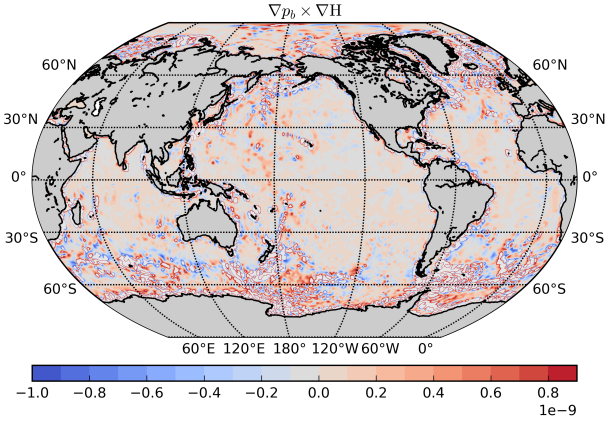

(c) $\nabla p_b \times \nabla H$

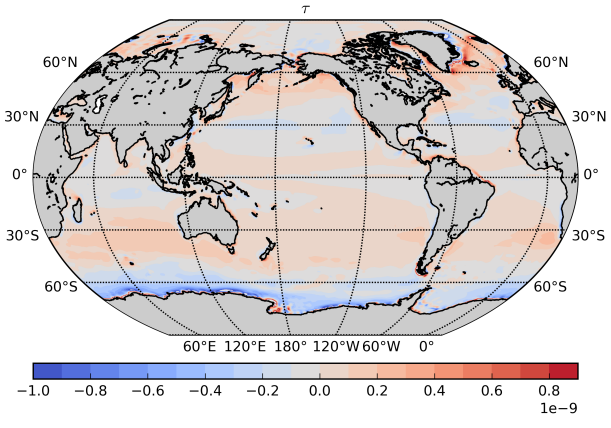

(d) $\nabla \times \tau$

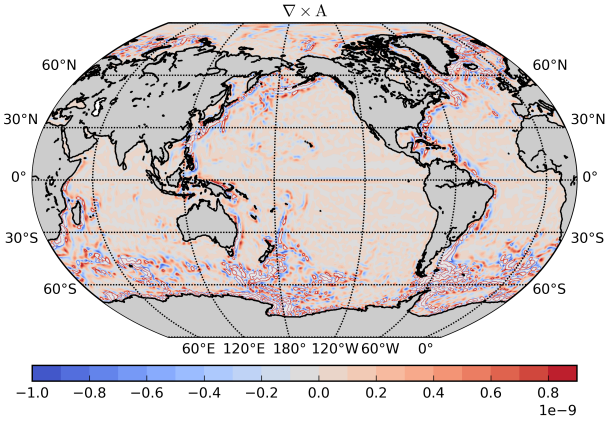

(e) $\nabla \times \mathbf{A}$

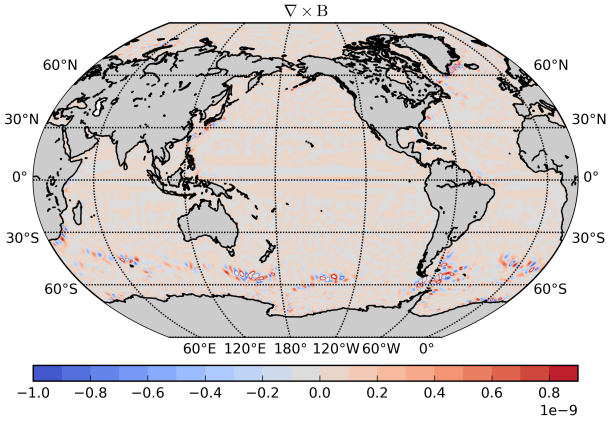

(f) $\nabla \times \mathbf{B}$

FIG. 1: The breakdown of the barotropic vorticity budget (ms^{-1}) over 1992-2013 in the ECCOv4 State Estimate.

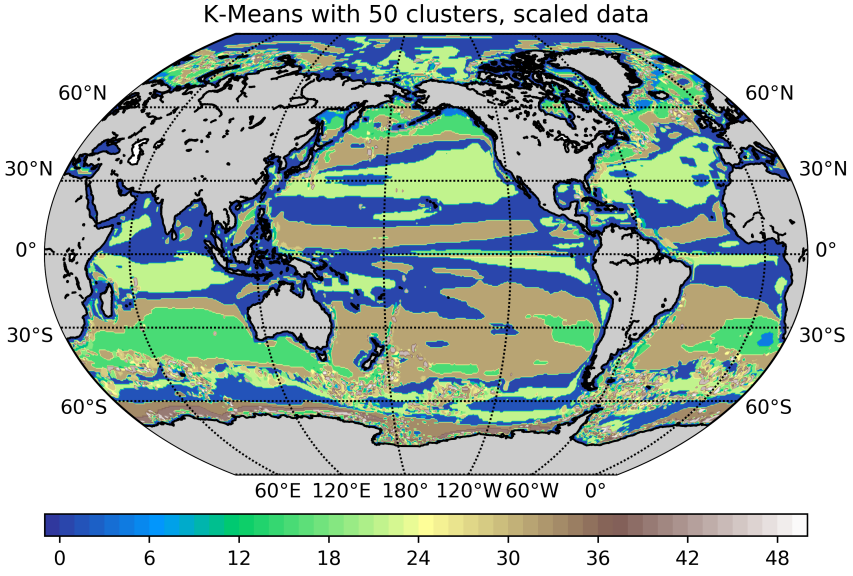

FIG. 2: The area selected by the clusters. The colors represent the clusters, and are in arbitrary order. The momentum dominated ocean region (55.6%, Figure 3a) is in dark blue, the Transition zone (17.6%, Figure 3c) is in light brown, the Subtropical Gyre ("Quasi-Sverdrup", 11.2% Figure3e in light green, the Subpolar gyre (6.6%, Figure 4a) is in gark green, the Southern Ocean gyre (2%, Figure 4c) in lighter blue and the remaining areas where the non-linear terms are large amounting to 6.3% of the world ocean and are presented in Figure 4e.)

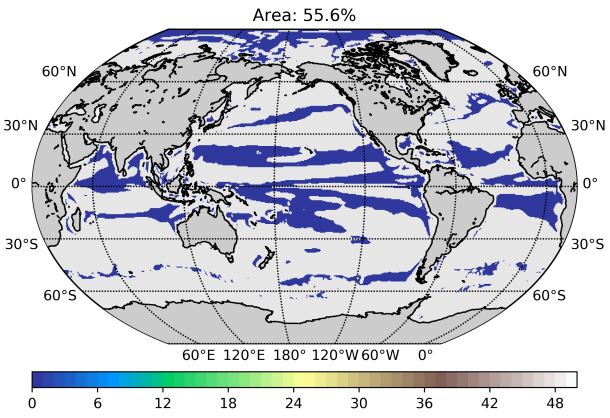

(a) Cluster 1: Depth coherent

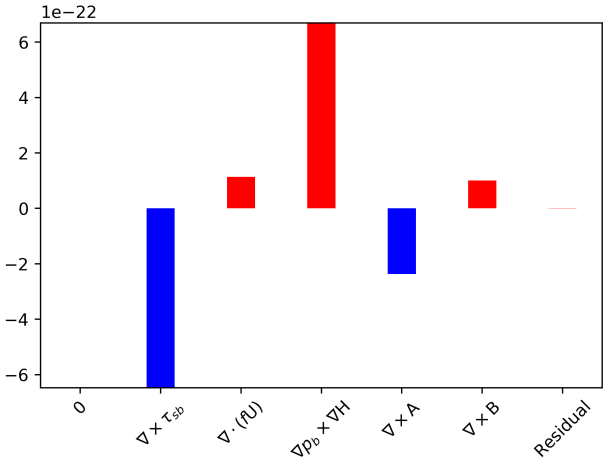

(b) Depth coherent: Area averaged histogram

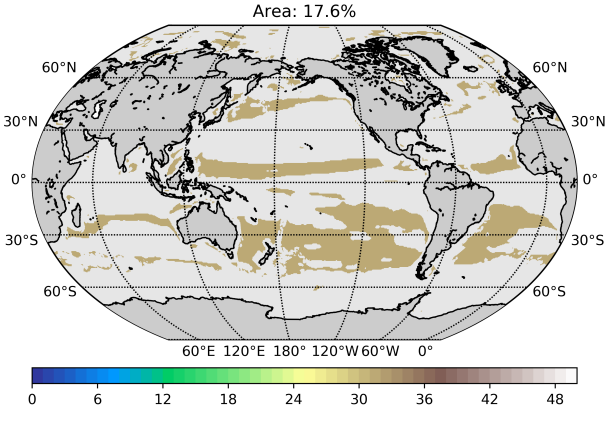

(c) Cluster 2: Transition Zone

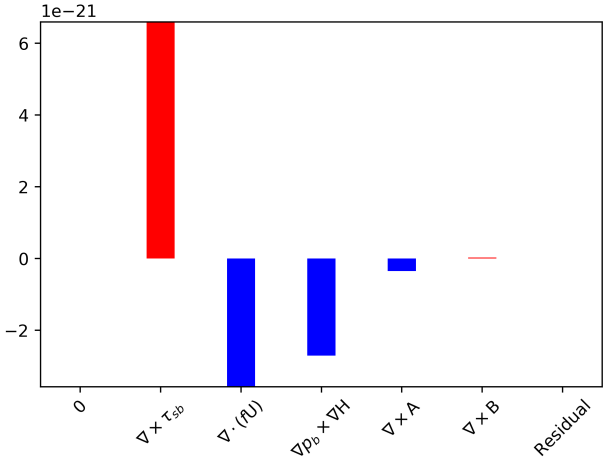

(d) Transition zone: Area averaged histogram

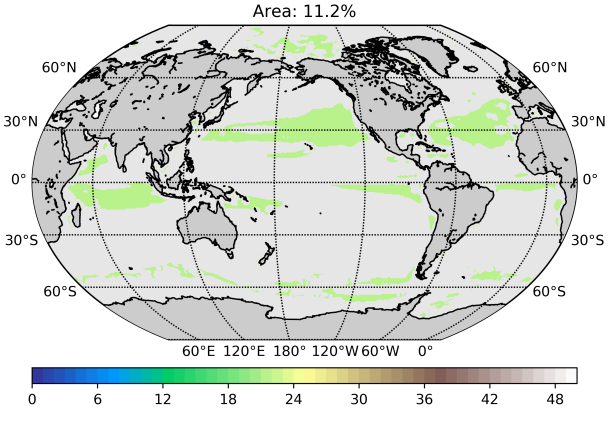

(e) Cluster 3: Subtropical gyre

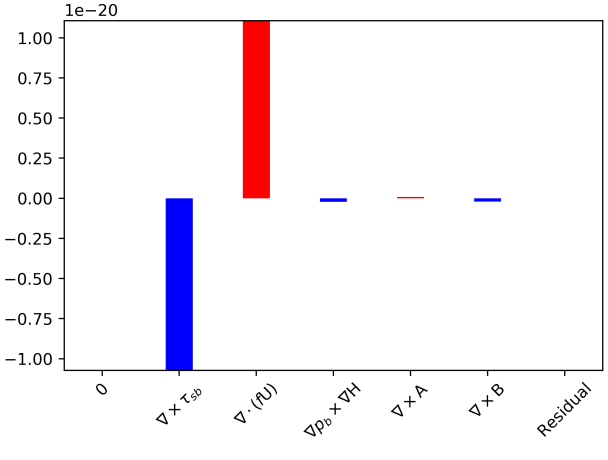

(f) Subtropical gyre: Area averaged histogram

FIG. 3: Maps of the selected locations (left) and corresponding area averaged histogram (right) of the terms in the BV equation. The colorbar is kept, but the color/ordering of the map are arbitrary. Colors in the barchart indicate if BV is added (red) or removed (blue).

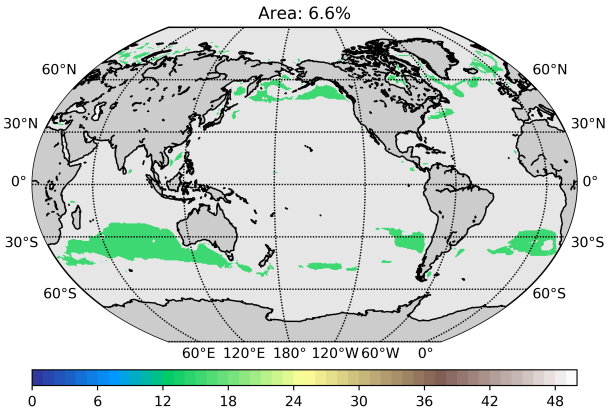

(a) Cluster 4: Subpolar gyre

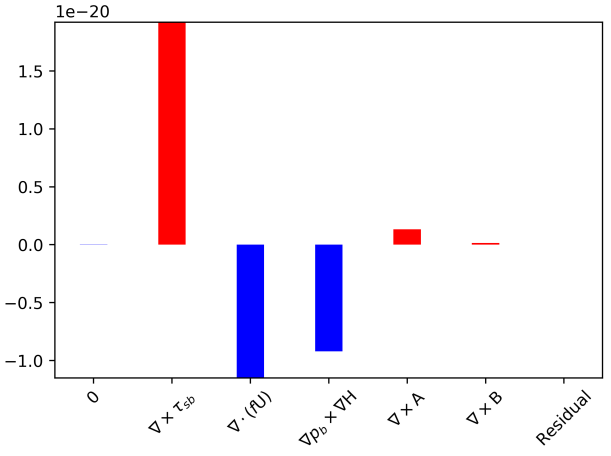

(b) Subpolar gyre: Area averaged histogram

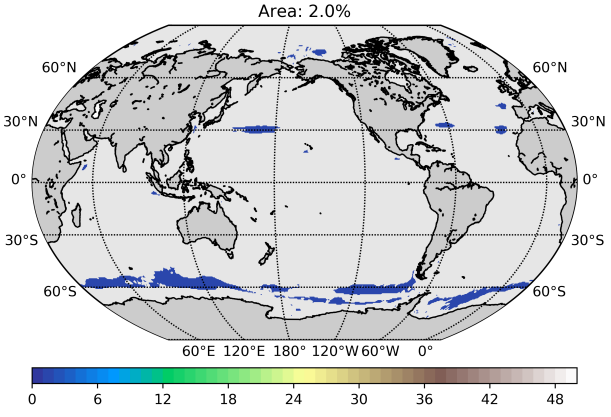

(c) Cluster 5: Southern Ocean gyre

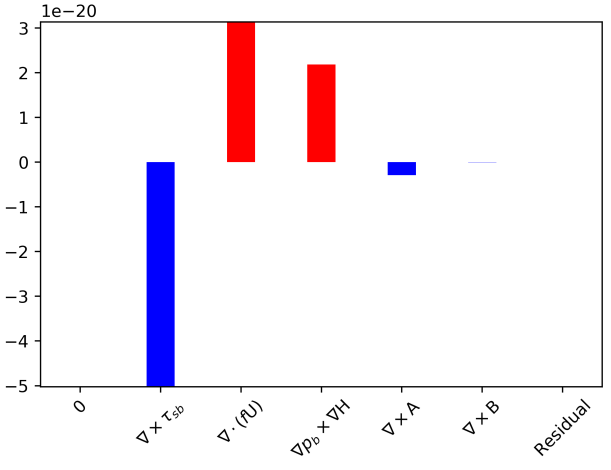

(d) Southern Ocean gyre: Area averaged histogram

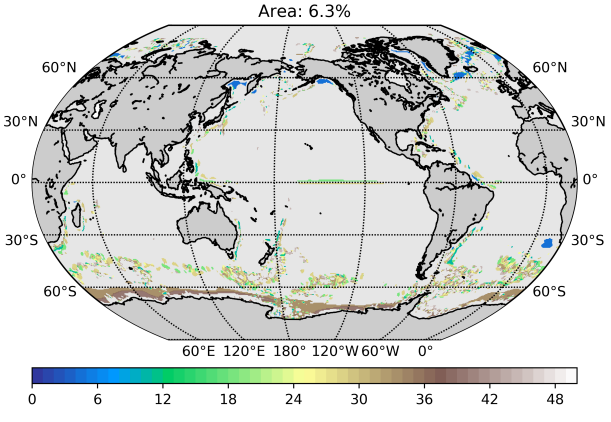

(e) Dominantly non-linear

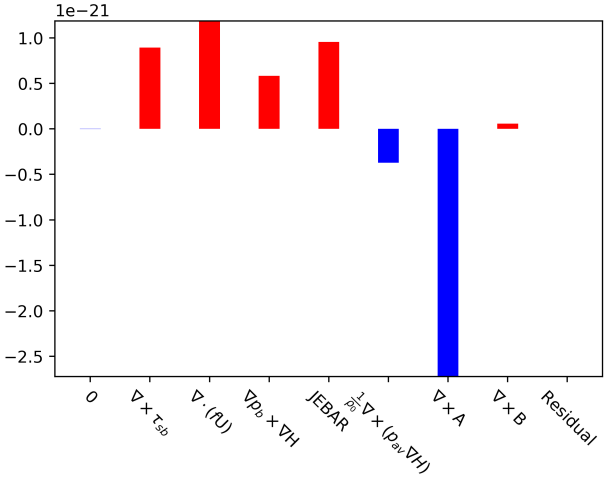

(f) Dominantly non-linear: Area averaged histogram

FIG. 4: Maps of the selected locations (left) and corresponding area averaged histogram (right) of the terms in the BV equation. The colorbar is kept, but the color/ordering of the map are arbitrary. Colors in the barchart indicate if BV is added (red) or removed (blue).

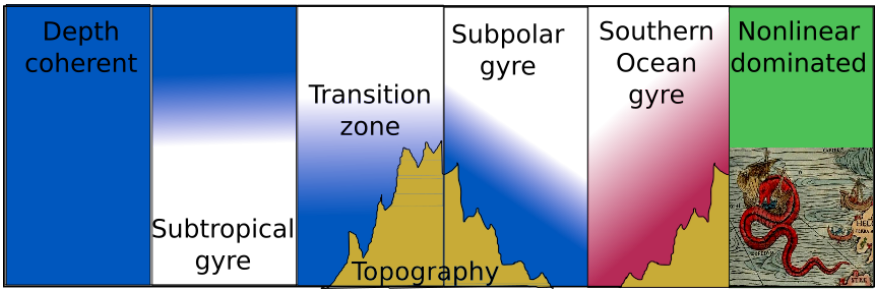

FIG. 5: Schematic of identified regions. The momentum dominated area implies a coherent vertical structure. The subtropical gyre is unique due to lack of BPT. The transition zone has a stronger momentum driven portion of the BPT, and topographic interactions begin to become important. The subpolar gyre has a stronger baroclinic component to the BPT and feels topography. The Southern Ocean gyre is like the subpolar, but with contributions of opposite sign. The remainder is dominated by non-linear contributions, and the barotropic interpretation is not appropriate.

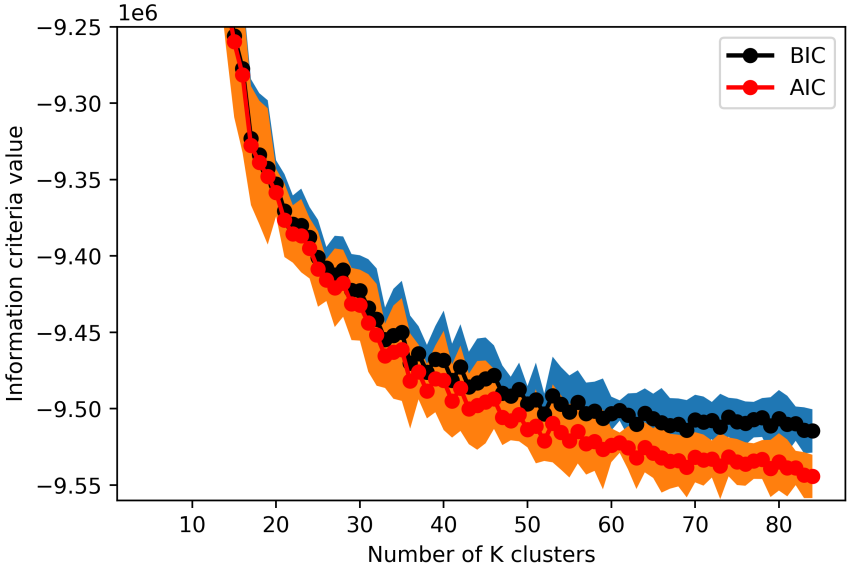

FIG. 6: The AIC and BIC asymptote and we choose a K of 50 for our analysis. Error bars represent 2σ, capturing the stochastic start seen of the algorithm.

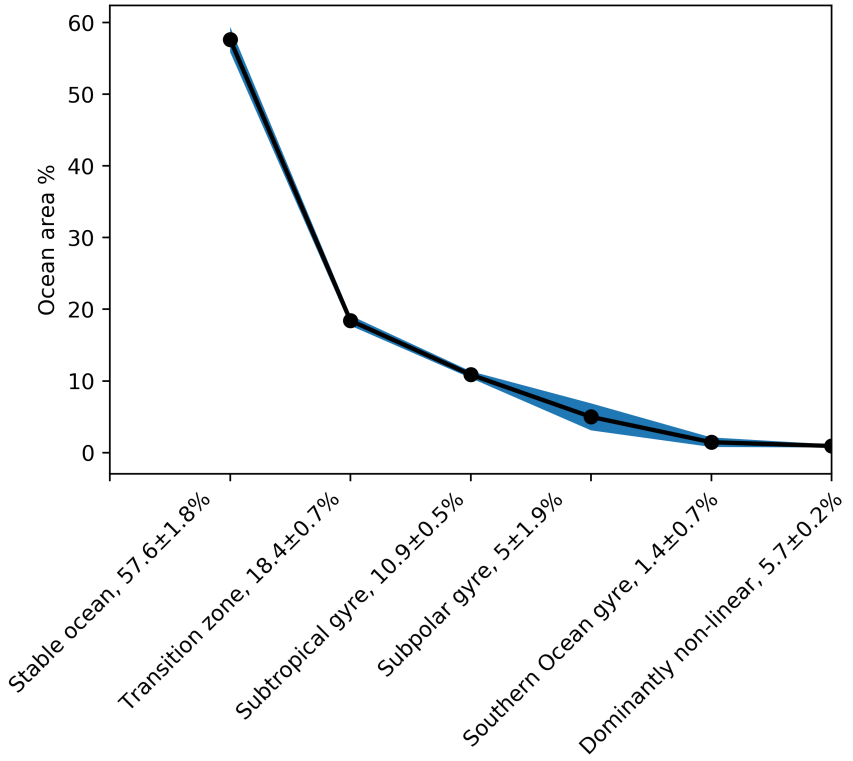

FIG. 7: The ocean area represented by the different areas from table 1, and 100 runs of the classification. Error bars represent 2σ, capturing the stochastic start seed of the classification algorithm. The final point "Dominantly non-linear" represents the remainder in the 45 clusters not shown.

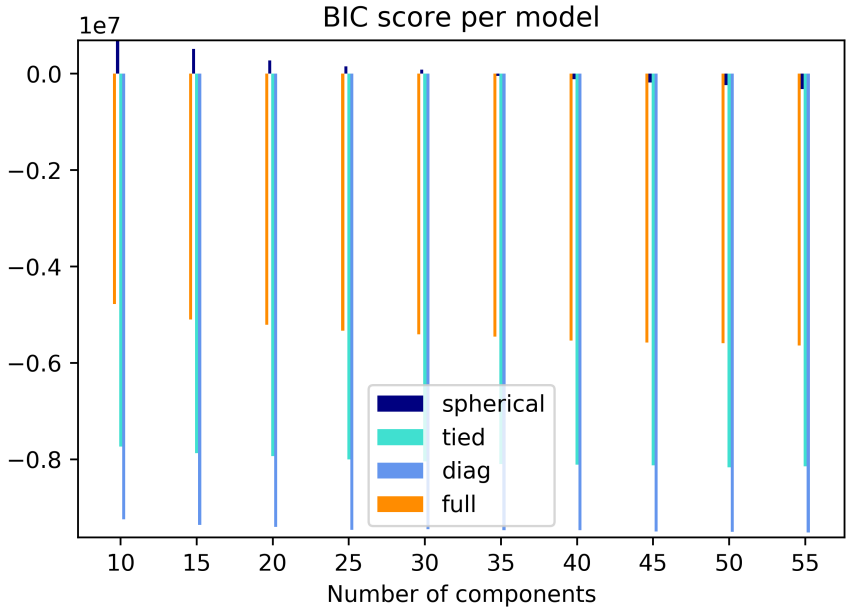

FIG. 8: Trying different covariance models to check the convergence.